Palladium Nanoparticle Formation Processes in Fluoropolymers by Thermal Decomposition of Organometallic Precursors

Journal:	*Physical Chemistry Chemical Physics*
Manuscript ID	CP-ART-08-2018-004997
Article Type:	Paper
Date Submitted by the Author:	06-Aug-2018
Complete List of Authors:	Zeng, Fan; Johns Hopkins University, Materials Science and Engineering Zhang, Dajie; Johns Hopkins University Applied Physics Laboratory Spicer, James; The Johns Hopkins University, Materials Science and Engineering

Journal Name

ARTICLE TYPE

Cite this: DOI: 10.1039/xxxxxxxxxx

Palladium Nanoparticle Formation Processes in Fluoropolymers by Thermal Decomposition of Organometallic Precursors

Fan W. Zeng,*[a] Dajie Zhang,[b] and James B. Spicer[a]

Received Date
Accepted Date

DOI: 10.1039/xxxxxxxxxx

www.rsc.org/journalname

Palladium nanoparticles were synthesized directly in solid fluoropolymer films by thermal decomposition of palladium acetylacetonate precursor molecularly infused in the fluoropolymer matrix. This chemical infusion synthesis technique was studied using transmission electron microscopy along with selective area electron diffraction to gain insight into the nucleation and growth of palladium nanoparticles. Formation of palladium nanoparticles can be correlated with defects in the polymer matrix as well as their associated free volume such that a relationship between average particle size and mean free volume fraction can be constructed. At low processing temperatures, the average particle radius increases monotonically with the processing time but more complicated variations occur for longer times. The growth of nanoparticles was interpreted using a modified diffusion-limited growth model. While nearly monodisperse nanoparticles dispersed throughout the polymer volume were obtained at low processing temperatures, surface percolation of nanoparticles was observed at relatively high temperatures owing to high precursor decomposition and diffusion rates.

1 Introduction

Polymer-based materials containing inorganic or organic nanostructures are termed polymer matrix nanocomposites (PMNCs). The use of nanostructures in a polymer can provide high performance materials that find applications in diverse fields, such as automobiles, aerospace components, sporting goods, packaging, and high-energy-density capacitors[1–7]. There are two preparation methods that have been used generally for synthesis of PMNCs[8–11]: (1) physical methods that involve direct mixing and melt processing of a filler with a polymer (melt compounding and film casting), (2) chemical methods that incorporate a filler or a filler precursor into monomers of a polymer matrix followed by polymerization (*in-situ* polymerization and *in-situ* sol-gel polymerization). Although these synthesis methods are well-developed, it is difficult to employ them with fluoropolymers since most of these materials are not melt-processable, cannot be dissolved easily, and can be dangerous to handle at ambient conditions when monomers are being used. Even so, numerous application possibilities for fluoropolymer-based PMNCs exist since these polymers have outstanding engineering properties—they are tough, chemically inert, and are able to withstand exposure to high temperatures (up to ~300 °C)[12]. For example, tungsten oxide nanoparticles embedded in poly(tetrafluoroethylene-co-hexafluoropropylene) (also known as fluorinated ethylene propylene or FEP) can be developed into a flexible and durable material that can automatically darken when exposed to ultraviolet light[13]. The most widely used method to synthesize fluoropolymer matrix-metal or metal oxide nanocomposites is a vapor phase co-deposition process[14,15] in which different loading of nanoparticles in the fluoropolymer can be achieved by controlling the deposition rates[16]. While this co-deposition technique is well-established, it is expensive and only a small amount of material can be produced. An alternative method, named chemical infusion, has been developed to provide a relatively low-cost and scalable route to synthesize nanoparticles in fluoropolymer films[17]. The essential processing steps include placing the fluoropolymer matrix along with a particle-precursor chemical in a vacuum reaction vessel, heating up the vessel to a desired temperature so that the precursor vaporizes and diffuses into the solid fluoropolymer matrix, and increasing the temperature so that the precursor molecules decompose and produce species that form nanoparticles. While this processing technique can potentially be used to synthesize multi-functional nanoparticles in the bulk of the fluoropolymer matrix[13,18], details of the synthesis process and the related mechanisms of nanoparticle formation are not well understood. This type of understanding is a critical prerequisite for designing and producing PMNC materials with desirable proper-

[a] *Department of Materials Science and Engineering, Johns Hopkins University, Baltimore, MD, 21218, USA; E-mail: fanwzeng@jhu.edu.*
[b] *Johns Hopkins University Applied Physics Laboratory, 11100 Johns Hopkins Road, Laurel, Maryland 20723, USA.*

ties.

The formation of nanoparticles in polymer solutions has been studied in depth owing to the development of advanced characterization techniques, such as *in-situ* liquid cell transmission electron microscopy and time-resolved *in-situ* small angle X-ray scattering[19–21]. In general, nanoparticle synthesis in solutions can be described using the classical LaMer burst mechanism[22–24]. The LaMer mechanism is divided into three stages: (1) the solute species in solution are supersaturated but no particles are present; (2) the concentration of solute reaches a critical level of supersaturation that drives rapid nucleation which partially relieves supersaturation; (3) nanoparticle growth occurs by incorporation of the remaining solute—there is almost no additional nucleation. The growth process can continue through Oswald ripening[25] resulting in particle size dispersity, and the characteristic particle size distribution is described in the Lifshitz-Slyozov-Wagner (LSW) theory[26,27]. At a later stage of the growth process, other particle growth phenomena can also occur, such as coalescence, orientated attachment, and intraparticle growth[28–31]. For synthesis of transition metal nanoparticles, a two-step mechanism, named Finke-Watzky mechanism, has been proposed[32]. The Finke-Watzky mechanism consists of slow continuous nucleation followed by autocatalytic surface growth ($A \rightarrow B$ followed by $A + B \rightarrow 2B$ where A is a general organometallic precursor and B is a nanocrystal). This mechanism has been shown to describe various nanoparticle systems, including platinum[33], iridium[34], and rhodium[35]. Similar to nanoparticle formation in solution, nanoparticle formation on the surface of a substrate via vapor deposition generally obeys the classical theory of heterogeneous nucleation on defects, and particle growth is mainly governed by diffusion of adsorbed atoms. The degree of applicability of this classical approach depends on the size of the nuclei. For those involving large critical nuclei, it describes the nucleation and growth process well since the macroscopic thermodynamic properties can be appropriately assigned to the nuclei. For small critical nuclei, statistical mechanical models have been developed[36,37] and validated experimentally for many material systems[38–42].

Although the chemical infusion technique used in this study is different from the wet chemistry or vapor deposition techniques in terms of synthesis procedures, we will show that its essential mechanism of nanoparticle formation can be interpreted by combining heterogeneous nucleation theory and various particle growth mechanisms. For the work presented in this study, palladium nanoparticles were grown in a semi-crystalline fluoropolymer using the chemical infusion technique, and the formation of palladium nanoparticles was studied by creating a series of samples that effectively captured particle size and distribution as a function of processing times and by analyzing these samples using transmission electron microscopy—imaging as well as selective area electron diffraction. Using related results, it is shown that the nucleation of nanoparticles can be connected to the free volume of polymer[43] (free volume is the difference between the specific volume and the specific volume of the crystalline phase[44–46]) and that the growth of the nanoparticles can be divided into four stages each with its own growth characteristics. Having established the essential aspects of the particle synthesis process, the effect of temperature as a processing variable on particle formation can be interpreted to understand widely differing spatial distributions of particles in polymer matrices.

2 Experimental

2.1 Materials

Commercially available palladium(II) acetylacetonate ($Pd(acac)_2$; 99% Pd; Sigma-Aldrich) was used as a precursor for preparing palladium nanoparticles. This precursor has a low decomposition temperature and has been used extensively for study of palladium deposition[47,48]. The palladium precursor was used in its as-received state without further preparation. A semicrystalline poly[tetrafluoroethylene-co-(perfluoropropyl vinyl ether)] (PFA; CS Hyde) was chosen as the polymer matrix. The surfaces of the PFA films were cleaned with acetone and deionized water prior to synthesis.

2.2 Synthesis of Palladium nanocomposites

Palladium nanocomposites (designated as Pd-PFA) were synthesized using a chemical infusion technique. The synthesis process was started by placing a $60 \times 100 \times 0.127\ mm^3$ PFA film in a glass reaction vessel along with ~30 mg of $Pd(acac)_2$ powder dispersed around the inner wall of the vessel. The reaction vessel was evacuated to ~160 mTorr in order to remove air from the vessel as well as volatiles from the PFA matrix. The vessel was heated in an oven for 2 hours at 140 $^\circ C$ to sublime/vaporize the $Pd(acac)_2$ precursor and allow the precursor to diffuse into the PFA matrix. Owing to the process used to synthesize the nanocomposites, there was a large volume of palladium precursor placed on the wall of the reaction vessel, and the precursor must vaporize and be transported a significant distance (up to 20 mm) to reach the polymer. As a result, it is necessary to hold the reaction vessel at the vaporization temperature for an appropriate amount of time—two hours was determined to be adequate in this material system. The temperature of the oven was then raised to 180 $^\circ C$ (the lowest temperature at which the decomposition of $Pd(acac)_2$ could be observed) and held for 0.25, 0.5, 0.75, 1, 2, 6, and 8 hours to induce precursor decomposition followed by nanoparticle formation. The reaction vessel was quickly transferred to a room temperature environment in order to arrest the particle-formation-state in the sample—Pd-PFA is very stable structurally at room temperature and this can inhibit various growth processes from occurring. A series of 7 different Pd-PFA films with various dwell times for decomposition was used to study the nucleation and growth of Pd particles in PFA. A separate set of Pd-PFA was synthesized at relatively high temperatures (220 $^\circ C$ and 240 $^\circ C$) and short processing time (~2 hours)—further particle growth was not observed after this processing time. The resulting nanocomposites were used to study the effect of temperature on particle formation.

2.3 Characterization

Transmission electron microscopy (TEM) images and selective area electron diffraction (SAED) patterns were obtained to provide particle size, particle distribution, average number density,

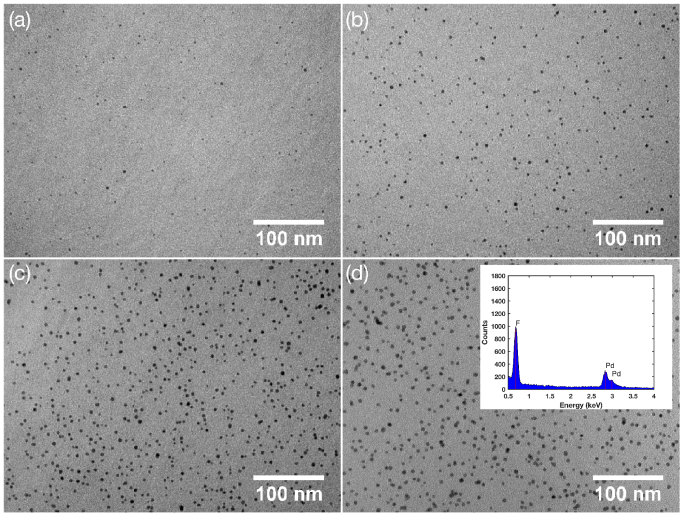

Fig. 1 Representative TEM images of Pd-PFA processed at 180 $^{\circ}C$ with dwell time = (a) 0.25, (b) 0.5, (c) 2, and (d) 8 hours. The inset shows an EDS spectrum of Pd-PFA.

and structural information about the Pd nanoparticles. Cross sectional samples ~100 nm in thickness were prepared using diamond microtome methods. Samples were then mounted on copper grids and imaged on a 100 kV Philips EM 420 transmission electron microscope. The point-to-point resolution of the TEM was 0.33 nm. Standard software (ImageJ) was used to analyze the TEM micrographs. An Oxford energy dispersive X-ray spectroscopy (EDS) detector was used for the elemental analysis.

3 Results and discussion

3.1 Nucleation and free volume

Representative TEM micrographs illustrating a systematic time-sequence for nanoparticle formation are shown in Fig. 1. The energy dispersive X-ray spectroscopy analysis (inset of Fig. 1) indicates the presence of palladium, and the detection of fluorine is resulted from the PFA matrix. These palladium nanoparticles are approximately spherical, and the particle number density as well as particle size appear to increase as the processing time increases. The nanoparticle number density was measured from the TEM micrographs, and its variation with time at 180 $^{\circ}C$ is shown in Fig. 2. Unlike the LaMer burst nucleation, in which the rate of nucleation is effectively infinite, the particle number density increases slowly over a period of about two hours. This slow nucleation can be attributed to the decomposition characteristics of $Pd(acac)_2$. The rate at which the palladium atoms arrive at the nucleation sites depends on the decomposition rate of the precursor and this will necessarily impact the nucleation process. The variation of particle number density in Fig. 2 can be best described by an exponential approach to a saturation value associated with a maximum particle number density. This is to be expected if a fixed and limited number of nucleation sites is present initially in the polymer. If the rate at which the nucleation sites become occupied by particles is given by the following:

$$\frac{dN}{dt} = \frac{I(N_0 - N)}{N_0} \tag{1}$$

where N is the number of sites occupied at time t, I is the nucleation rate, and N_0 is the maximum number of available sites, then the number of particles as a function of time is:

$$N = N_0 \left[1 - exp\left(-\frac{It}{N_0}\right)\right]. \tag{2}$$

Equation 2 can be used to fit the experimental results in Fig. 2 with the result shown where N_0 and I were taken to be 4.23×10^{16} cm^{-3} and 1.23×10^{13} $cm^{-3}s^{-1}$, respectively.

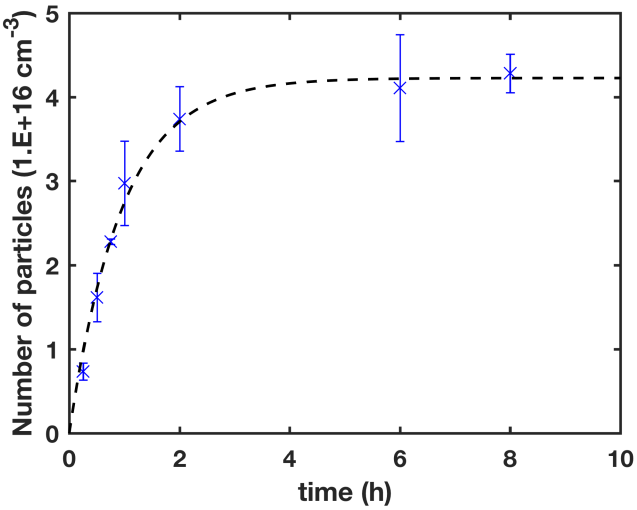

Fig. 2 Average palladium particle number density at various dwell time for decomposition temperature of 180 $^{\circ}C$. The error bars represent the overall distribution of the data. Dashed line represents the best fit to Eq. (2).

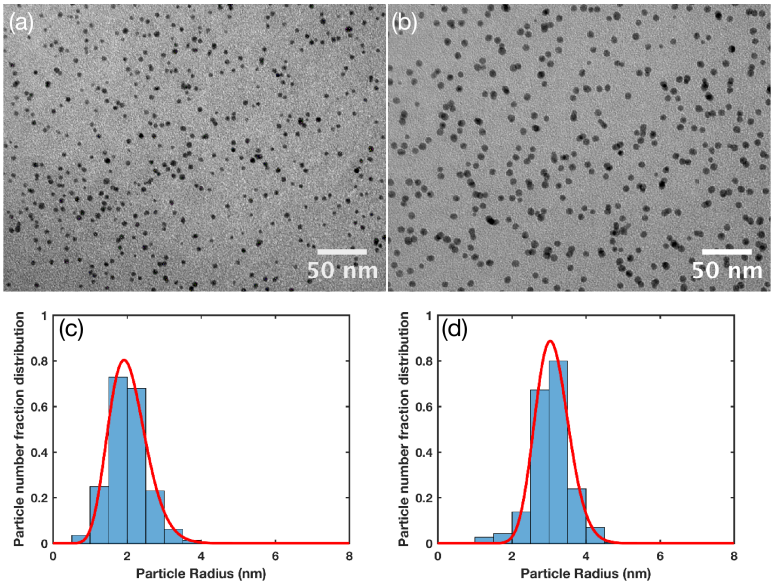

Fig. 3 Representative TEM images of saturation concentration of Pd nanoparticles in PFA processed at (a) 180 $^{\circ}C$ for 8 hours and at (b) 220 $^{\circ}C$ for 2 hours; (c) and (d) showing their corresponding particle size distributions. Solid lines are curve fit based on Eq. (3).

Palladium nanocomposites were also synthesized at a relatively high temperature (220 $^{\circ}C$), while keeping the other experimental conditions the same. Although the nucleation rate at this high processing temperature was not determined, it generally requires less time for the particle number density to reach its saturation level when compared to materials processed at relatively low temperatures. The nucleation rate likely increases with temperature since the decomposition rate of the palladium precursor (and hence the incident rate of palladium atoms) also increases as temperature increases[38–40,47,48]. Figure 3 shows representative TEM images of Pd-PFA processed at 180 and at 220 $^{\circ}C$ as well as their corresponding particle size distributions (PSDs). The bin-width, $W = 0.5$ nm, was chosen based on Sturge's method[49] where $W = (R_{max} - R_{min})/(1 + log_2 M)$, where R_{max} and R_{min} are the maximum and minimum particle radius and M is the number of particles. It should be noted that detection of particles less than 0.5 nm in radius was difficult owing to insufficient contrast between the background structure originating from the polymer matrix and any small particles that might be present. The radius of the nanoparticle ranges from 0.6 to 3.8 nm for Pd-PFA processed at 180 $^{\circ}C$ and from 0.6 to 4.8 nm for materials processed at 220 $^{\circ}C$. Neither a Gaussian nor a left-skewed distribution (which is a characteristic shape of the LSW theory for Ostwald ripening[50]) was found in any of the Pd-PFA samples. The Pd particle size distribution, $P(R)$, follows a model based on the Schulz-Flory distribution[51], which is given by

$$P(R) = \frac{z}{R_{ave}\Gamma(z)}\left(\frac{zR}{R_{ave}}\right)^{z-1} exp\left(-\frac{zR}{R_{ave}}\right) \quad (3)$$

where R_{ave} is the average particle radius, and z is related to the particle polydispersity (pp) by $pp = z^{-1/2}$ and can be referred to as the width of the Schulz-Flory distribution[52]. While this gamma distribution has been used on an *ad hoc* basis in many similar material systems previously[13,51–54], it is equivalent to the free volume density distributions found for a variety of polymer systems[55–58] suggesting that there is some connection between particle size and free volume. The PSDs were fit using a non-linear least squares curve fitting routine based on Eq. (3), and the results are shown in Fig. 3 (c) and (d). A one-sided Kolmogorov-Smirnov test was used to make goodness of fit analysis, and the results suggested that the Schulz-Flory gamma distribution fits the particle size distributions well. The average particle radius was determined to be 2.0 nm and 3.1 nm for Pd-PFA processed at 180 $^{\circ}C$ and at 220 $^{\circ}C$, respectively. The values of z were determined to be 16 and 47, which correspond to polydispersity of 0.25 and 0.15, for material processed at 180 $^{\circ}C$ and at 220 $^{\circ}C$, respectively. Higher processing temperature resulted in larger nanoparticles and narrower width of particle size distribution. Apparently, the precursor molecules do not all decompose at once at the decomposition temperature (180 $^{\circ}C$ and 220 $^{\circ}C$). The ones that do decompose can release palladium atoms that nucleate at nearby sites or contribute to growth of existing particles, and the ones that have not decomposed can continue the diffusion process until a concentration equilibrium is reached. More precursor molecules can dissolve in the PFA matrix at 220 $^{\circ}C$ than at 180 $^{\circ}C$, which results in larger nanoparticles at higher temperature.

Regardless of the processing temperature, the Pd nanoparticles seem to form throughout the bulk of the polymer matrix. However, when considering heterogeneous nucleation, the preferred sites for nucleation should reside on the defects or imperfections in the polymer matrix with the result that the density of defects should somehow correlate with the apparent particle number density. The saturation particle number densities observed at different processing temperatures appear to be similar (Fig. 3 (a) and (b) contain approximately 450 and 375 nanoparticles, respectively) suggesting that particle nucleation possibly occurs on the existing defect sites in the PFA matrix.

Defects and imperfections in polymers have distinct definitions.

For a semi-crystalline polymer, defects can be chain disorder in the crystalline region, interface between the crystalline and amorphous regions, and poor chain packing with voids in the amorphous region. These defects can be related to the free volume of the polymer. In particular, Spaepen has proposed that the fraction of defect sites n in a system can be determined via a relation of the form[43]:

$$n = \Delta f exp\left(-\frac{\gamma v}{v_f}\right) \quad (4)$$

where Δf is the fraction of the sample volume in which potential defect sites can be found, γ is a geometrical factor that takes into account the overlap between the neighboring free volume (ranges between 0.5 and 1), v is volume, and v_f is free volume. Various studies have shown that the fractional free volume ($\frac{v_f}{v}$) increases linearly as temperature increases[56,59,60]. Consequently, according to Eq. (4), the volume fraction of defects, and hence volume fraction of preferential nucleation sites, should increase as temperature increases. The implication is that Pd-PFA processed at 220 $^{\circ}C$ should have higher fractional defect volume than materials processed at 180 $^{\circ}C$. This increase in fractional defect volume can result in additional nucleation sites, relatively bigger defect size, or a combination of both effects. However, it is unlikely that higher processing temperature will result in additional nucleation sites since the saturation number concentration of the nanoparticles in Pd-PFA processed at 220 $^{\circ}C$ is similar to (and slightly lower than) that in materials processed at 180 $^{\circ}C$ (Fig. 3). The increase in fractional defect volume may largely come from the growth of defect size. Regardless, the increase in defect volume will allow additional precursor molecules to diffuse into the polymer matrix so that the nanoparticle size should increase accordingly. To verify this, the fractional defect volume n was calculated using Eq. (4) letting $\frac{v}{v_f} = 6.1$ for $T = 220$ $^{\circ}C$ and 7.6 for $T = 180$ $^{\circ}C$ (these values were obtained from a diffusion study for a Pd(acac)$_2$-PFA system[61]). Assuming Δf remains unchanged and the geometrical factor $\gamma = 0.5$ (or 1), Pd-PFA processed at 220 $^{\circ}C$ has an n value approximately 2.1 (or 4.5) times higher than for material processed at 180 $^{\circ}C$. Compared to the total particle volume, which can be determined by assuming all the nanoparticles are spherically shaped, Pd-PFA processed at 220 $^{\circ}C$ has a total particle volume value 2.6 times higher than material processed at 180 $^{\circ}C$. This difference in total particle volume is comparable to the difference in fractional defect volume, which was calculated to range from 2.1 to 4.5. In fact, the fractional defect volume difference equals the total particle volume difference when the geometrical factor $\gamma = 0.63$ is used.

On the basis of the observed relation between particle size and polymer defect volume, we conclude that the volume fraction of defects is directly related to the maximum particle volume fraction. By equating Eq. (4) to the volume fraction of spherical nanoparticles, a relation between the average particle radius and the mean fractional free volume f_m can be expressed as:

$$R_{ave} = \left[\frac{3\Delta f}{4\pi\rho_n} exp\left(-\frac{\gamma}{f_m}\right)\right]^{1/3} \quad (5)$$

where ρ_n is the particle number density. This result indicates that the average particle radius can be calculated from the mean fractional free volume, or vice versa. For instance, if $\gamma = 0.63$, $\Delta f = 1$, and $\rho_n = 4.3 \times 10^{-5}$ nm^{-3} (an estimated particle number density based on TEM micrographs), nanoparticles can be grown to an average size ranging from 2.6 to 8.7 nm in diameter when the mean fractional free volume varies from 0.08 to 0.15, which are typical f_m values for fluoropolymers based on the measurements using positron annihilation lifetime spectroscopy[56,59,60].

3.2 Particle Growth

Decomposition of an organometallic precursor molecule could yield either a metal complex or a metal atom. As a result, there are two separate pathways for formation of stable nanoclusters from precursor molecules: one is to bond as complex metal ions then a reduction to occur, or reduce first and then bond as atoms. The latter is more likely since the thermogravimetric studies have indicated that the thermal decomposition of Pd(acac)$_2$ is a single-step process that yields Pd atoms and 2acac molecules[48]. After forming stable nanoclusters, the growth rate is directly related to the total flux of atoms joining a cluster[62]. However, the total flux cannot be easily determined since the concentration of atoms at a distance from the center of the particle is not known. This problem can be solved, at steady state, using the lattice approximation, where a constant density of particles is assumed to be regularly distributed on a square lattice[63,64]. Based on these assumptions, Henry and Meunier numerically solved the rate equation showing that the growth of metal clusters on insulators can be expressed by a power law[62,65]. However, steady state growth conditions do not hold in our material system since the average concentration of species available for particle growth diminishes over time. In our case, the nanoparticle growth is analogous to diffusion-limited growth. Previous studies have shown that, during diffusion-limited growth, the average solute concentration $\langle C \rangle$ in a diffusion field can be expressed approximately as follows[66,67]:

$$\langle C \rangle = (C_0 - C_f) exp\left(-\frac{A_D t}{\pi r_f^2}\right) + C_f, \quad (6)$$

indicating that the temporal variation of the mean solute concentration depends on the initial C_0 and final C_f concentrations as well as the spacing between nucleation sites r_f and the parameter A_D that is linearly proportional to the diffusion coefficient of the growth species. For our palladium nanocomposites, there are two possible mechanisms for precursor-decomposition-and-particle-growth. Growth of Pd nanoparticles at the early stage can occur by thermal decomposition of Pd precursor followed by capture of diffusing Pd atoms or by direct impingement of Pd precursor molecules on the existing nanoclusters followed by autocatalytic surface growth[32]. The temporal variations of particle size should differ between these two mechanisms (decomposition-and-transport versus transport-and-decomposition) since the diffusion coefficients of palladium atoms and palladium precursor molecules as well as the decomposition rates will likely differ. Despite the differences, the growth of nanoparticles can be estimated by modifying Eq. (6). Since the amount of solute that

contributes to the particle growth is $1-\langle C\rangle/C_0$, convolving it with the precursor decomposition probability function yields an equation that can adequately describe the nanoparticle growth. This equation is given as follows:

$$\langle \bar{R} \rangle = \left\{ \left[1 - \frac{C_0 - C_f}{C_0} exp\left(-\frac{A_D t}{\pi r_f^2} \right) - \frac{C_f}{C_0} \right] * S(t) \right\}^{1/3}, \quad (7)$$

where $\langle \bar{R} \rangle$ is the average particle radius normalized by the maximum average particle radius, $S(t)$ is the precursor decomposition probability function, and the asterisk indicates convolution with respect to time. For the transport-and-decomposition case, the particle-mediated catalytic decomposition is likely a rapid process so that $S(t)$ can be represented by a Dirac delta function. For the decomposition-and-transport case, the probability of thermal decomposition of precursor is not known. However, a previous study has shown that 50 mg of $Pd(acac)_2$ required approximately 4 hours to be fully decomposed in a nitrogen atmosphere at 190 $^\circ C$[47]. As a result, the probability function for thermal decomposition of precursor is likely a broad Gaussian distribution under the assumption of normality. For our material system, since the nucleation and growth rates appear to be highest when the processing time is ~0.5 hour and greatly diminish after ~1 hour, the mean and the standard deviation of the Gaussian probability density function can be assumed to be 0.5.

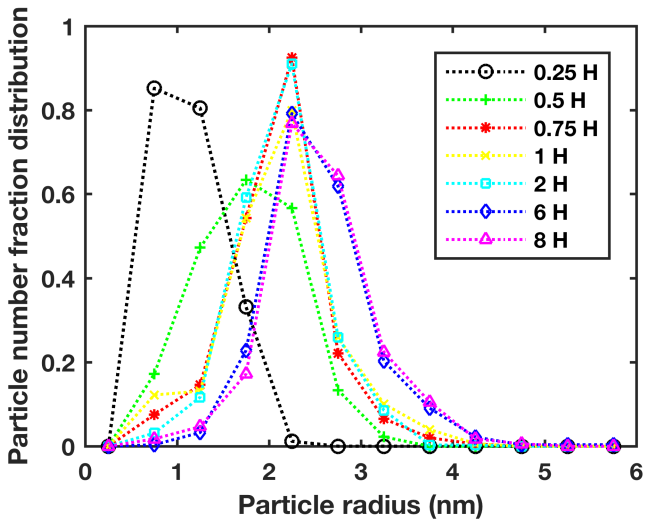

Fig. 4 Particle size, population distribution of Pd-PFA synthesized at 180 $^\circ C$ with various dwell time.

Figure 4 shows the time evolution of particle size distributions of Pd-PFA processed at 180 $^\circ C$. The average particle radii were determined by fitting the particle size distributions with Eq. (3). Figure 5 shows the change of particle radius as a function of processing times, where the error bars represent $\pm$ 1 standard deviation of the radii. In order to use Eq. (7) to describe the growth of the nanoparticles, a couple of parameters (C_f and r_f) have to be adequately determined beforehand. First, the final concentration of the growth species, C_f, can be assumed to be 0 since no further particle growth was observed when the dwell time exceeded 8 hours. Second, the radius of the diffusion field, r_f, was taken to be 9 nm, and this value was determined by treating each nanoparticle as a diffusion sink and by employing Voronoi approximation. Specifically, Voronoi tessellation was first performed on the TEM micrographs, and then the area of each Voronoi polygon was approximated by a circular region with an area equal to the polygon. Figure 6 shows a TEM image and its corresponding Voronoi diagram where five circles are displayed to demonstrate the area approximation. Finally, the average value of the radii of the circular regions was taken to be r_f. It should be noted that this Voronoi approximation is a two dimensional approach to estimate the radius of the diffusion field. If the average inter-particle distance is 18 nm ($2r_f$) in a 100 nm thick sample, the TEM images would show approximately 6 particle layers on top of each other. As a result, this rough estimation of r_f represents the smallest average first neighbor shell distance of nanoparticles. Under these appropriate assumption and approximation, the growth of the nanoparticles can now be fit using Eq. (7). Since both growth mechanisms (decomposition-and-transport versus transport-and-decomposition) are expected to take place during the reaction processes, the precursor decomposition probability function, $S(t)$, is taken to be a Dirac delta function and a Gaussian probability density function. Using a least-squares fitting method, Eq. (7) appears to fit the growth of particle radius well when the precursor decomposition probability function equals to the Dirac delta function (Fig. 5 dashed line). In contrast, a poor fit was found when the precursor decomposition probability function is taken to be the Gaussian function (Fig. 5 dotted line). These results suggest that the transport-and-decomposition process dominates over the decomposition-and-transport process. In the case of $S(t)$

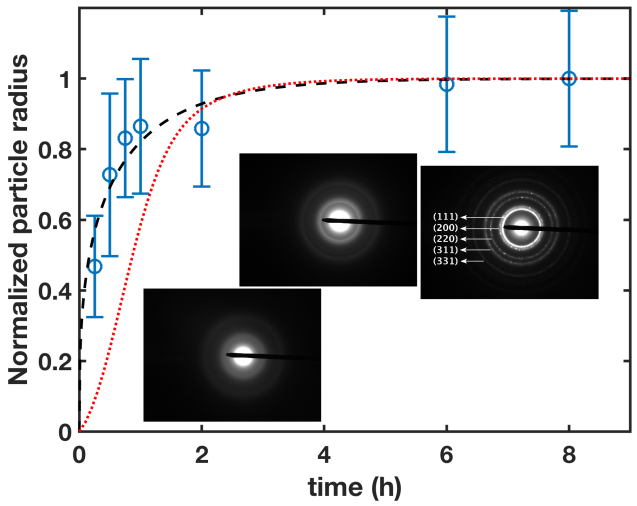

Fig. 5 Evolution of normalized palladium particle radius at decomposition temperature of 180 $^\circ C$. The error bars represent $\pm$ 1 standard deviation. Dashed line is the curve fit based on Eq. (7) with $S(t)$ equals a Dirac delta function; the sum of squared errors of the curve fit is 0.0211. Dotted line is the curve fit based on Eq. (7) with $S(t)$ equals a Gaussian probability density function. Inset figures depict representative SAED patterns of Pd-PFA with short (left), medium (middle). and long (right) processing times.

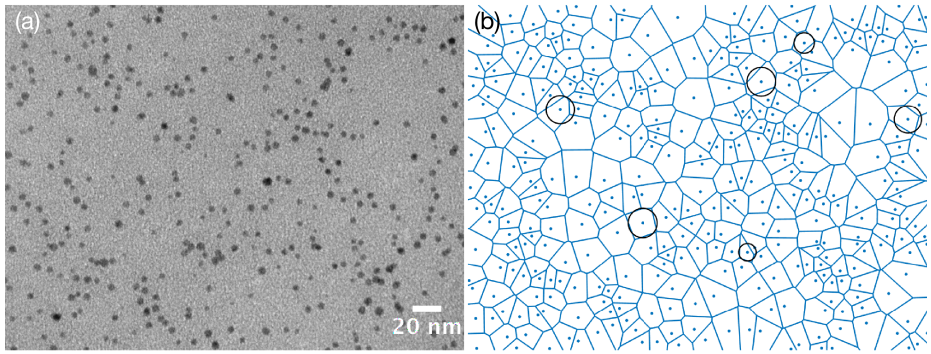

Fig. 6 (a) Representative TEM image of Pd-PFA synthesized at 180 $^{\circ}C$ for 8 hours and (b) its corresponding Voronoi diagram. The spaces closest to the diffusion sinks, represented by the Voronoi polygons, are approximated by circular regions with areas equal to those of the polygons. For clarity, selective circular regions are displayed in the diagram.

equals to the Dirac delta function, the parameter A_D was found to be 205.5 nm^2/hour, and this parameter is linearly proportional to the diffusion coefficient D such that $A_D = \alpha D$ where α is a coefficient of proportionality[66]. Unfortunately, the values of α and D cannot be determined independently from a single fit. However, it is possible to estimate the diffusion coefficients (and the activation energy) by studying an additional set of particle growth behavior at a different processing temperature and by assuming α is independent of temperature.

It is interesting to note that the nanoparticle growth presented in this study (Fig. 5) is similar to the nanocrystal growth proposed by Wang *et al.*[68], which includes classical nucleation and growth followed by aggregative nucleation and growth. The authors illustrated that the classical regime usually produces primary nanocrystals (often ranged in 1 to 3 nm in diameter), and that regime is followed by a second induction and growth period associated with primary nanocrystals diffusion and coalescence (aggregative nucleation and growth). In the final regime, Oswald ripening may or may not be present. The authors also suggested that the aggregative-growth kinetics can be fit using a modified Kolmogorov-Johnson-Mehl-Avrami (KJMA) method. However, since the fitting parameters (a "rate" parameter and the Avrami exponent) possess no physical meaning for nanoparticle formation[69], the fitting results will only be useful in comparison studies[70]. For this reason, even though the KJMA expression can fit the nanoparticle growth profile in Fig. 5 reasonably well (but not as well as Eq. (7)), the fitting results are not provided here.

While interpretation of the particle growth is challenging, we will attempt to describe its growth process by dividing Fig. 5 into four different stages. In stage I ($0 < t < 1$ H), the particles have a fast growth rate since the concentration of species available for inclusion in particles is high at the beginning. Both decomposition-and-transport and transport-and-decomposition processes take place in this stage, but the transport-and-decomposition process likely dominates. In stage II ($1 < t < 2$ H), the average particle size is approximately unchanged, and one possible explanation is that the Pd nanoparticles begin to crystallize at this stage. During crystallization, atoms in nanoparticles arrange themselves in a close-packed fashion causing a decrease in the sizes of the nanoparticles. However, this decrease in particle size might be accommodated by the growth species that have yet to be bonded to the nanoparticles. As a result, the variation of particle size is small in this stage. Although the crystallization temperature of palladium is up to $\sim$500 $^{\circ}C$[71], crystallization of nanoparticles is known to be size dependent—the smaller the particle the lower the crystallization temperature[72–74]. Electron diffraction measurements were performed on the Pd-PFA samples with short (0.75 H), medium (2 H), and long (6 H) processing times, and representative SAED patterns are shown in Fig. 5. As expected, when the processing time is short, the SAED patterns exhibit diffuse rings (left), indicating that the Pd nanoparticles are amorphous. As the processing time increases, the diffraction rings are more distinct (middle). At long processing times, the SAED patterns (right) show relatively sharp rings indicating that the Pd nanoparticles are crystalline[75]. These Pd nanoparticles are polycrystalline, and the SAED patterns exhibit five sharp rings assigned to (111), (200), (220), (311), and (331) lattice planes with spacing 2.2 Å (111), 1.9 Å (200), 1.3 Å (220), 1.2 Å (311), and 0.9 Å (331) of face centered cubic Pd. In stage III ($2 < t < 6$ H), crystallization continues accompanied by a small growth rate. This slow growth could be related to exhaustion of the remaining growth species as well as particle co-

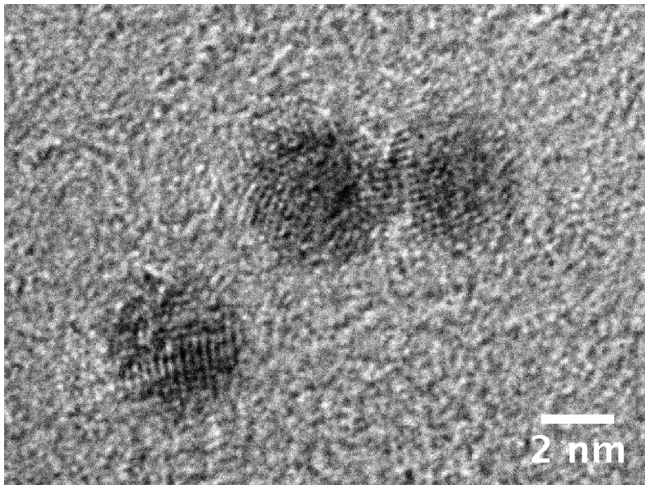

Fig. 7 High resolution TEM image showing the oriented attachment of two palladium nanoparticles. Materials were synthesized at 180$^{\circ}C$ for 8 hours.

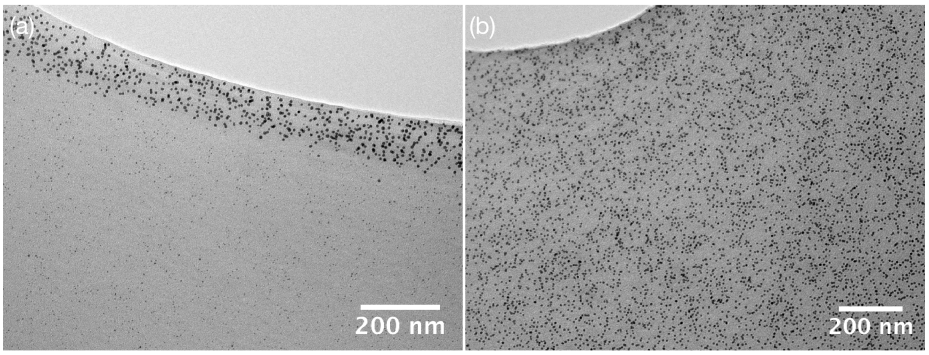

Fig. 8 TEM images of near surface region of Pd-PFA processed at (a) 240 $^{\circ}C$ for 2 hours and (b) 220$^{\circ}C$ for 2 hours.

alescence and oriented attachment (aggregative growth). Occasionally, if the nanoparticles are in close proximity to each other, they can merge and combine into one large particle in order to reduce their surface area. However, this phenomenon is greatly hindered because of the network structure of the polymer chains. Figure 7 shows a particular case of two Pd nanoparticles that have undergone oriented attachment—the lattice fringes at the particle boundary were perfectly aligned. The shape of the PSD is also an indication of aggregative growth of nanoparticles. Grillo *et al.* described the growth of platinum nanoparticles in atomic layer deposition and devised a dynamic model that accounts for single atoms and nanoparticles diffusion and coalescence[76]. In that coalescence model, the characteristic PSD exhibits a right-skewed distribution. This characteristic shape of the PSD is also found in our nanoparticle system, especially at the later stage of particle growth (Fig. 4). Neither Oswald ripening nor other types of particle growth was observed in stage IV ($7 > t > 8$ H). The optical properties of the Pd-PFA films remained unchanged even after prolonged processing (up to 18 H). The driving force for Ostwald ripening is the difference in chemical potential between particles of difference sizes. However, Ostwald ripening is likely suppressed since the disperse phase (nanoparticles) has a very low solubility in the continuous phase (polymer matrix). Also, further aggregative growth is unlikely to occur since the nanoparticles can be stabilized by the polymer matrix via steric interaction. While metal nanoparticles have strong van der Waals forces and tend to aggregate when in inert nonpolar media, aggregation is usually prevented by coating the nanoparticles with a tightly bound polymer[77]. The Pd nanoparticles synthesized in this study were not coated with any surfactants. However, these nanoparticles were grown on or in the vicinity of the fluoroalkyl chains of the PFA matrix, and the fluoroalkyl end-capped oligomers are known to be able to encapsulate and stabilize fine metal particles[78].

3.3 Surface percolation of nanoparticles

At a low processing temperature, the four stages of nanoparticle growth are quite evident. However, the time needed to accomplish each stage at higher processing temperatures might be less than at 180 $^{\circ}C$. It appears that these nanocomposites can be synthesized in shorter periods of time at higher temperatures. In order to determine the highest temperature that will retain homogeneous particle size and spatial distributions throughout the bulk of the polymer matrix, Pd-PFAs were synthesized at elevated temperatures. However, when the processing temperature was increased to 240 $^{\circ}C$, surface percolation of nanoparticles was observed, and this result is shown by the TEM image in Fig. 8 (a). In contrast, Pd-PFA synthesized at 220 $^{\circ}C$ displays similar particle number densities at the surface as are found in the bulk (see Fig. 8 (b)). Although high particle densities in the near surface region have been observed previously with multiple infusions[18], in this work a single infusion at high temperature showed a clear distinction between surface and bulk nanoparticles densities. This is important since we demonstrated that surface-loaded nanocomposites can be synthesized without extended processing. The radius of the nanoparticles in the bulk ranged from 1 to 2 nm, and the bulk exhibits a relatively low particle number concentration compared to the surface. The average radius of the near-surface nanoparticles is approximately 4 nm, more than twice that of bulk nanoparticles. These near-surface nanoparticles are often interconnected so that a randomly percolated structure is formed. While the polymer surface has slightly higher free volume than the bulk[79], it is unlikely that the small difference in free volume is a critical contributing factor for the surface percolation of nanoparticles since PMNCs processed at low temperatures exhibit rather uniform particle number densities in the entire sample. Alternatively, high processing temperatures ($\geq$ 240 $^{\circ}C$) cause high precursor decomposition rates, and the resulting palladium atoms build up near the surface since there is not enough time for the precursor concentration to reach equilibrium inside and outside of the polymer matrix—the surface of the polymer have higher precursor concentration than the bulk. Therefore, a dense layer of particles is formed near surface when the processing temperature is relatively high. In addition, the subsurface layer of the Pd particles are formed at the early stage of the decomposition process, and this dense layer of particles obstructs further diffusion of precursor molecules (that have not yet decomposed) into the polymer matrix and consequently relatively small particles are formed in the bulk.

4 Conclusion

In this study, the formation of palladium nanoparticles in PFA using thermal decomposition of organometallic precursor molecules dispersed inside of a PFA matrix was studied. Detailed TEM

studies indicated that the nucleation and growth of palladium nanoparticles in the PFA matrix depends strongly on the processing temperature and the structural characteristics of the polymer matrix. Heterogeneous nucleation of palladium nanoparticles on polymer defects was considered, and it was correlated to the free volume of the polymer matrix. Predictions were in quantitative agreement with experiment suggesting that nucleation occurs preferentially in the defect/free volume of the polymer matrix. A simple relation between the mean free volume fraction of the polymer and the average particle size was derived. The temporal evolution of the particle radius was interpreted using a modified diffusion-limited growth model. In addition, a four-stage particle growth process was illustrated, which can be summarized as (1) fast growth, (2) crystallization, (3) aggregative growth, and (4) stabilization by steric hindrance. The growth duration of each stage can be shortened by processing at elevated temperatures, and the average particle size increases with temperature. However, when the synthesis temperature is sufficiently high, near-surface percolation of nanoparticles occurs because of high precursor decomposition and diffusion rates. The results obtained here demonstrate that the fundamental limitations of growing nanoparticles in a solid polymer matrix are the processing temperature and the morphology of the polymer matrix. By carefully adjusting the processing temperature, not only monodisperse nanoparticles can be obtained but surface-loaded nanocomposites can also be synthesized. More importantly, it is possible to manipulate the nanoparticle size and spatial distributions by varying the free volume of the polymer matrix.

Conflicts of interest

There are no conflicts to declare.

Acknowledgements

The authors gratefully acknowledge support by the National Science Foundation through the CMMI Division under Award Number 1462151.

References

1 J. Njuguna and K. Pielichowski, *Advanced Engineering Materials*, 2003, **5**, 769–778.
2 A. K. Naskar, J. K. Keum and R. G. Boeman, *Nature Publishing Group*, 2016, **11**, 1026.
3 A. Rasheed and F. A. Khalid, International Symposium on Advanced Materials, 2014, p. 012009.
4 F. Gao, *Materials Today*, 2004, **7**, 50–55.
5 *Advances in polymer nanocomposites : types and applications*, ed. Gao F., Woodhead, 2012, p. 651.
6 G. Wang, Y. Huang, Y. Wang, P. Jiang and X. Huang, *Physical Chemistry Chemical Physics*, 2017, **19**, 21058–21068.
7 E. Kar, N. Bose, S. Das, N. Mukherjee and S. Mukherjee, *Physical Chemistry Chemical Physics*, 2015, **17**, 22784–22798.
8 S. Li, M. Meng Lin, M. S. Toprak, D. K. Kim and M. Muhammed, *Nano reviews*, 2010, **1**, 5214.
9 F. Hussain, *Journal of Composite Materials*, 2006, **40**, 1511–1575.
10 M. Oliveira and A. V. Machado, *Nanocomposites: synthesis, characterization and applications*, 2013, 1–22.
11 F.-L. Mi, S.-J. Wu, W.-Q. Zhong and C.-Y. Huang, *Physical Chemistry Chemical Physics*, 2015, **17**, 21243–21253.
12 S. Ebnesajjad, *Applied Plastics Engineering Handbook*, William Andrew, 2011, ch. 4, pp. 49–60.
13 T. J. DeJournett and J. B. Spicer, *Solar Energy Materials and Solar Cells*, 2014, **120**, 102–108.
14 U. Schurmann, W. Hartung, H. Takele, V. Zaporojtchenko and F. Faupel, *Nanotechnology*, 2005, **16**, 1078.
15 L. Rosenthal, H. Greve, V. Zaporojtchenko, T. Strunskus, F. Faupel and M. Bonitz, *Journal of Applied Physics*, 2013, **114**, 044305.
16 A. Biswas, Z. Marton, J. Kanzow, J. Kruse, V. Zaporojtchenko, T. Strunskus, M. Czank and F. Faupel, *Solid State Phenomena*, 2003, **94**, 285–294.
17 T. Koloski and T. Vargo, *Polymer and inorganic-organic hybrid composites and methods for making same*, 1999.
18 J. Spicer, K. See, Y. Katsumi, D. Zhang, J. Brupbacher, T. Vargo, R. M. Hall and I. Technologies, NSTI-Nanotech 2006, 2006, pp. 789–792.
19 T. J. Woehl, J. E. Evans, I. Arslan, W. D. Ristenpart and N. D. Browning, *ACS Nano*, 2012, **6**, 8599–8610.
20 B. L. Caetano, C. V. Santilli, F. Meneau, V. Briois and S. H. Pulcinelli, *The Journal of Physical Chemistry C*, 2011, **115**, 4404–4412.
21 J. Polte, R. Erler, A. F. ThuĬnemann, S. Sokolov, T. T. Ahner, K. Rademann, F. Emmerling and R. Kraehnert, *ACS Nano*, 2010, **4**, 1076–1082.
22 V. K. LaMer and R. H. Dinegar, *Journal of the American Chemical Society*, 1950, **72**, 4847–4854.
23 V. K. LaMer, *Industrial & Engineering Chemistry*, 1952, **44**, 1270–1277.
24 A. Baronov, K. Bufkin, D. W. Shaw, B. L. Johnson and D. L. Patrick, *Physical Chemistry Chemical Physics*, 2015, **17**, 20846–20852.
25 W. Ostwald, *Chemical physics*, 1900, **34**, 495.
26 I. Lifshitz and V. Slyozov, *Journal of Physics and Chemistry of Solids*, 1961, **19**, 35–50.
27 C. Z. Wagner, *Angew. Phys. Chem.*, 1961, **65**, 581–591.
28 H. Zheng, R. K. Smith, Y.-w. Jun, C. Kisielowski, U. Dahmen and A. P. Alivisatos, *Science*, 2009, **324**, 1309.
29 R. L. Penn and J. F. Banfield, *Geochim. Cosmochim. Acta*, 1999, **63**, 1549.
30 X. Peng, L. Manna, W. Yang, J. Wickham, E. Scher, A. Kadavanich and A. P. Alivisatos, *Nature*, 2000, **404**, 59.
31 M. José-Yacamán, C. Gutierrez-Wing, M. Miki, . D.-Q. Yang, â. K. N. Piyakis and E. Sacher, *J. Phys. Chem. B*, 2005, **109**, 9703.
32 M. A. Watzky and R. G. Finke, *Chem. Mater.*, 1997, **9**, 3083.
33 C. Besson, E. E. Finney and R. G. Finke, *Journal of American Chemical Society*, 2005, **127**, 8179.
34 M. A. Watzky, E. E. Finney and R. G. Finke, *Journal of the American Chemical Society*, 2008, **130**, 11959–11969.

35 S. Yao, Y. Yuan, C. Xiao, W. Li, Y. Kou, P. J. Dyson, N. Yan, H. Asakura, K. Teramura and T. Tanaka, *The Journal of Physical Chemistry C*, 2012, **116**, 15076–15086.

36 D. Walton, *The Journal of Chemical Physics*, 1962, **37**, 2182–2188.

37 A. Milchev, *ChemTexts*, 2016, **2**, 4.

38 J. Robins and T. Rhodin, *Surface Science*, 1964, **2**, 346–355.

39 J. Hamilton and P. Logel, *Thin Solid Films*, 1973, **16**, 49–63.

40 V. Robinson and J. Robins, *Thin Solid Films*, 1974, **20**, 155–175.

41 J. A. Venables, G. D. T. Spiller and M. Hanbucken, *Rep. Prog. Phys.*, 1984, **47**, 399–459.

42 M. Zinke-Allmang, L. C. Feldman and M. H. Grabow, *Surface Science Reports*, 1992, **16**, 377–463.

43 F. Spaepen, *Acta Metallurgica*, 1977, **25**, 407–415.

44 A. K. Doolittle, *Journal of Applied Physics*, 1951, **22**, 1471.

45 T. G. Fox and P. J. Flory, *Journal of Applied Physics*, 1950, **21**, 581.

46 T. G. Fox and P. J. Flory, *The Journal of Physical Chemistry*, 1951, **55**, 221–234.

47 V. Cominos and a. Gavriilidis, *The European Physical Journal Applied Physics*, 2001, **15**, 23–33.

48 B. Janković and S. Mentus, *Journal of Thermal Analysis and Calorimetry*, 2008, **94**, 395–403.

49 H. A. Sturges, *Journal of American Statistical Association*, 1926, 65.

50 A. Baldan, *Journal of Materials Science*, 2002, **37**, 2171–2202.

51 K. Nakamura, T. Kawabata and Y. Mori, *Powder Technology*, 2003, **131**, 120–128.

52 R. Bienert, F. Emmerling and A. F. Thünemann, *Analytical and Bioanalytical Chemistry*, 2009, **395**, 1651–1660.

53 T. J. Dejournett and J. B. Spicer, *J. Phys. Chem. C*, 2014, **118**, 9820.

54 T. J. DeJournett and J. B. Spicer, *Physical Chemistry Chemical Physics*, 2013, **15**, 19753.

55 J. Liu, Q. Deng and Y. C. Jean, *Macromolecules*, 1993, **26**, 7149–7155.

56 G. Dlubek, A. Sen Gupta, J. Pionteck, R. Häßler, R. Krause-Rehberg, H. Kaspar and K. H. Lochhaas, *Polymer*, 2005, **46**, 6075.

57 R. A. L. Vallée, N. Tomczak, L. Kuipers, G. J. Vancso and N. F. van Hulst, *Physical Review Letters*, 2003, **91**, 038301.

58 R. A. L. Vallée, M. Cotlet, M. Van Der Auweraer, J. Hofkens, K. Müllen and F. C. De Schryver, *Journal of the American Chemical Society*, 2004, **126**, 2296–2297.

59 G. Dlubek, M. A. Alam, K. Saarinen, J. Stejny and H. M. Fretwell, *ACTA PHYSICA POLONICA A*, 1999, **95**, 521.

60 G. Nter Dlubek, J. Rgen Pionteck, K. Rätzke, J. Kruse and F. Faupel, *Macromolecules*, 2008, **41**, 6125.

61 F. W. Zeng, D. Zhang and J. B. Spicer, *Journal of Inorganic and Organometallic Polymers and Materials*, 2018, 1–9.

62 C. R. Henry, *Crystal Research and Technology*, 1998, **33**, 1119–1140.

63 K. Routledge and M. Stowell, *Thin Solid Films*, 1970, **6**, 407–421.

64 M. J. Stowell, *Philosophical Magazine*, 1972, **26**, 349–360.

65 C. R. Henry and M. Meunier, *Vacuum*, 1998, **50**, 157–163.

66 J. B. Spicer and Y. Dikmelik, *Acta Materialia*, 2009, **57**, 1459–1465.

67 D. Turnbull, *Solid State Physics: Advances in Research and Applications*, Academic Press, New York, 1956, ch. 3, p. 226.

68 F. Wang, V. N. Richards, S. P. Shields and W. E. Buhro, *Chemistry of Materials*, 2014, **26**, 5.

69 E. E. Finney and R. G. Finke, *Chem. Mater*, 2009, **21**, 4692–4705.

70 S. P. Shields, V. N. Richards and W. E. Buhro, *Chem. Mater*, 2010, **22**, 3212–3225.

71 *Refractory Metals and Alloys IV: Research and Development - Google Books*, ed. R. I. Jaffee, Science, 1967, p. 758.

72 M. Attarian Shandiz, A. Safaei, S. Sanjabi and Z. Barber, *Journal of Physics and Chemistry of Solids*, 2007, **68**, 1396–1399.

73 P. Puri and V. Yang, *J. Phys. Chem. C*, 2007, **111**, 11776.

74 B. Chen, G. H. Ten Brink, G. Palasantzas and B. J. Kooi, *Scientific Reports*, 2016, **6**, 39546.

75 W. Lu, B. Wang, K. Wang, X. Wang and J. G. Hou, *Langmuir*, 2003, **19**, 5887.

76 F. Grillo, H. V. Bui, J. A. Moulijn, M. T. Kreutzer and J. Ruud Van Ommen, *Journal of Physical Chemistry Letters*, 2017, **8**, 975.

77 Y. Min, M. Akbulut, K. Kristiansen, Y. Golan and J. Israelachvili, *Nature Materials*, 2008, **7**, 527–538.

78 H. Sawada, *Handbook of Fluoropolymer Science and Technology*, John Wiley & Sons, Inc., Hoboken, NJ, USA, 2014, pp. 57–79.

79 Y. Jean, J. Zhang, H. Chen, Y. Li and G. Liu, *Spectrochimica Acta Part A: Molecular and Biomolecular Spectroscopy*, 2005, **61**, 1683–1691.

Physical Chemistry Chemical Physics